Study of π-π scattering amplitudes in the reaction $\pi^+p \to \Delta^{++}\pi^0\pi^0$ at 8.0 GeV

N. M. Cason, P. E. Cannata,* A. E. Baumbaugh,† J. M. Bishop, N. N. Biswas,
L. J. Dauwe, V. P. Kenney, R. C. Ruchti, and W. D. Shephard
University of Notre Dame, Notre Dame, Indiana 46556

J. M. Watson
Argonne National Laboratory, Argonne, Illinois 60439
(Received 11 April 1983)

An experiment studying the reaction $\pi^+p \to \Delta^{++}\pi^0\pi^0$ using the Argonne National Laboratory 1.5-m streamer chamber combined with a lead-glass hodoscope is described. The data were analyzed in terms of $\pi^+\pi^- \to \pi^0\pi^0$ scattering, and the details of the extrapolation to the pole are discussed. An energy-independent amplitude analysis from threshold to 2.3 GeV is presented. In this analysis the $f^0(1270)$, the $h^0(2040)$, and a $J^P=2^+$ state at 1.8 GeV with a width of 0.280 GeV are observed. The amplitude ambiguity arising from analyses of $\pi^+\pi^- \to \pi^+\pi^-$ data in the 1.6-GeV region is resolved. An energy-dependent phase-shift analysis from 1.0 to 1.5 GeV is presented.

I. INTRODUCTION

The π-π interaction has long been a subject of intense theoretical and experimental investigation.[1] The subject is of such interest because of the fundamental nature of the interaction and because of the light it sheds on the study of meson spectroscopy and hence the quark-antiquark (q-$\bar{q}$) interaction.

Most of the experimental information on the π-π interaction has come from the study[2-11] of the $\pi^+\pi^-$ final state because of the great experimental difficulty in studying neutral pions. The experiments[12-19] which have studied the $\pi^0\pi^0$ final state have generally suffered from low statistics and/or poor angular acceptance. In addition, these latter experiments have generally given information on the π-π scattering amplitude only in the low-energy region.

The incentive for doing a high-statistics $\pi^0\pi^0$ experiment with good angular acceptance over a wide mass range comes from the fact that the $\pi^0\pi^0$ system must be in a state of even angular momentum and even isospin. This means that the analysis of $\pi^0\pi^0$ data is simpler than that for $\pi^+\pi^-$ data (for which both even and odd angular momenta and isospins may be present). The isospin amplitudes occur in a different linear combination for $\pi^+\pi^- \to \pi^0\pi^0$ scattering than for $\pi^+\pi^- \to \pi^+\pi^-$ scattering and thus the ambiguities which arise in the amplitude analyses of $\pi^+\pi^-$ data can be resolved. In this paper we describe such an experiment which we have carried out. Some aspects of the data analysis have been published previously.[20-24]

II. EXPERIMENTAL PROCEDURE

The experiment was performed at the Argonne National Laboratory zero-gradient synchrotron (ZGS) using the 1.5-m streamer chamber combined with a 68-element lead-glass hodoscope to detect the γ's from the decay of π^0's. The experimental layout is shown in Fig. 1. Six proportional wire chambers (PWC's) with 2-mm spacing were used to measure the angle and position of incident 8.0-GeV/c π^+ mesons on a 30.5-cm-long, 3.8-cm-diameter liquid hydrogen target located within the sensitive volume of the streamer chamber. A scintillation-counter hodoscope with 3-mm resolution was placed at the momentum slit to measure the beam momentum to an accuracy of 0.28% [full width at half maximum (FWHM)]. Two threshold Čerenkov counters were used to select pions in the unseparated beam (which consisted of 96.6% protons). The beam was confined to a spot size 2.2 cm (vertically) by 3.2 cm (horizontally) by a series of coincidence counters and anticoincidence hole counters located in the beam.

The construction, calibration, monitoring, and performance of the lead-glass hodoscope have been described in detail elsewhere.[24] Basically, the hodoscope consisted of 68 lead-glass blocks each of dimension $8.9\times8.9\times33.0$ cm long arranged in a brick-wall fashion and located just downstream from the streamer-chamber magnet as shown in Figs. 2(A) and 2(B). The 3-in. phototubes used thus required magnetic shielding. The hodoscope elements were calibrated using positrons of various energies in the beam, and were monitored using an argon flash tube and fiber optics. The hodoscope had an energy resolution of $16\%/\sqrt{E}$ (FWHM) (for E in GeV) and a position resolu-

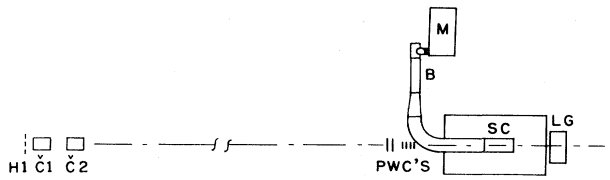

FIG. 1. Experimental layout showing the streamer chamber (SC) with its associated Marx generator (M) and Blumlein line (B); the lead-glass hodoscope (LG); the beam-measuring proportional wire chambers (PWC's); the momentum-measuring hodoscope (H1); and the Čerenkov counters (C1 and C2).

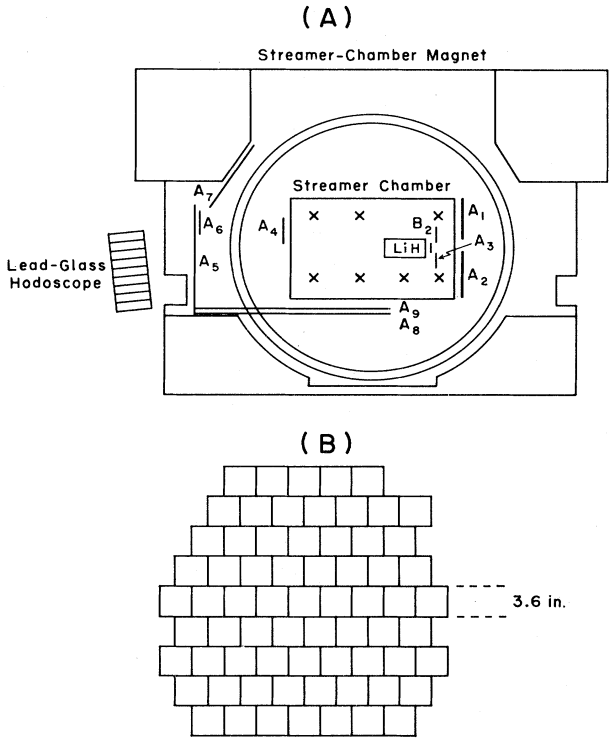

FIG. 2.(A) Arrangement of the streamer chamber inside the magnet with the liquid hydrogen target (LiH), the beam-defining counter B_2, the trigger anticoincidence counters (A_1—A_9) and the lead-glass hodoscope. (B) Beam's-eye view of the lead-glass hodoscope showing the brick-wall construction.

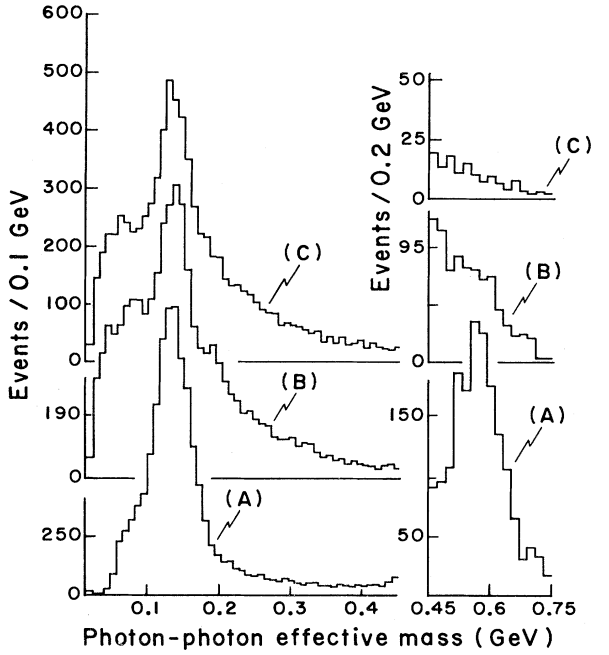

FIG. 3. The photon-photon effective mass spectrum for two- (A), three- (B), and four-γ (C) events.

tion[25] which varied, depending on the position of the γ, between 0.6 and 2.5 cm (σ). Shown in Fig. 3(A) are the π^0 and η^0 signals as observed in the detector for events in which two γ's hit the hodoscope. Similar distributions are shown in Figs. 3(B) and 3(C) for events in which three and four γ's, respectively, were detected.

The trigger for the experiment was optimized using Monte Carlo studies for the reaction $\pi^+ p \to \Delta^{++}\pi^0\pi^0$, and consisted of three parts: first, a π^+ beam particle was required to enter the hydrogen target using the various coincidence, anticoincidence, and Čerenkov counters located upstream from the target; second, since events of interest contained two low-momentum positive particles which bent upward in the streamer-chamber magnet, a system of veto counters located in the bottom of the streamer chamber and downstream from the streamer chamber was used to discriminate against events with negative particles and/or fast forward particles of either charge; and third, anode outputs from all the lead-glass blocks not on the periphery of the hodoscope were added linearly and a resulting pulse height corresponding to an energy deposit greater than 3.6 GeV was required.

Data were taken in four runs. The trigger rate was approximately 5×10^{-4} triggers per incident pion, or 1.7×10^{-5} triggers per incident positive particle. During the run the beam flux was adjusted to about 180×10^3 particles per pulse yielding an average of about two events per pulse. Some 400 000 triggers with three views of streamer-chamber photographs of the charged particles and with associated electronic information from the PWC system, the lead-glass hodoscope, and the latched beam-momentum counters were obtained. Constant on-line monitoring of the electronic equipment as well as the data acquisition was carried out using a Varian 620/*i* computer.

III. DATA REDUCTION

The streamer-chamber film was scanned for two-prong events, and these events were then digitized using both film-plane and image-plane measuring machines. After studying a sample of all two-prong events, scanning criteria were developed which would select Δ^{++} events produced with low four-momentum transfer, $|t|$, from the target proton. These criteria, developed using Monte Carlo simulations, required that both tracks have projected momentum less than 0.95 GeV and that at least one track have projected momentum less than 0.55 GeV. Some 100 000 events were measured on image-plane measuring machines and then processed by the geometric-reconstruction program TVGP.[26] The reconstructed events were then merged with the electronic data to obtain beam track angle, momentum, and position information as well as lead-glass information. After primary vertex position determination, obtained by extrapolating the charged tracks and the beam track into the liquid hydrogen target, neutral tracks were constructed using the lead-glass energy and position measurements. The brick-wall design and granularity of the hodoscope were such that a single pho-

ton could deposit energy in clusters of up to three blocks; low-energy π^0's had a minimum opening angle such that the energy deposit could be distributed in a cluster larger than three blocks; and high-energy π^0's (>3.6 GeV) could have both decay γ's contained within a three-block cluster. Therefore, on the basis of size and energy deposit of the clusters, they were divided into photon clusters, π^0 clusters, and ambiguous clusters. Further details of this neutral-track construction are described in Ref. 24.

Events with between one and four energy clusters in the lead glass were tested for kinematic consistency with a variety of possible final states using the program SQUAW.[27] Final states of interest are

$$\pi^+ p \to p\pi^+\pi^0\pi^0 , \quad (1)$$

$$\pi^+ p \to p\pi^+\pi^0 , \quad (2)$$

and

$$\pi^+ p \to n\pi^+\pi^+\pi^0 . \quad (3)$$

In addition, fits involving an η^0 replacing a π^0 were tested as were fits with three final-state π^0's. These latter event samples will not be discussed in this paper.

Overall missing-mass-squared distributions for one-, two-, three-, and four-cluster events are shown in Fig. 4. For the one-cluster events [Fig. 4(a)] the cluster is assumed to originate from a π^0 since the cluster spreads over more than three blocks or its energy is high enough that the small cluster can encompass both decay photons. Thus the missing mass for events of reaction (1) should peak at the π^0 mass. The two-cluster missing-mass distribution [Fig. 4(b)] shown is for events where the combined pair of clusters is consistent with a π^0, and thus should also peak at the missing π^0 mass for events of reaction (1). For the three-cluster events [Fig. 4(c)] two of the clusters are consistent with being decay γ's from a single π^0 and the third cluster can originate from a π^0, so the missing mass for reaction (1) should be zero. And finally, for the four-cluster sample [Fig. 4(d)], the clusters are consistent with decay γ's from two separate π^0's, and the missing mass for reaction (1) should again be zero. In each case, there is a peaking of the distribution at the expected position. Events in these peaks for which the appropriate γ-γ effective mass also is consistent with the π^0 mass (see Fig. 3) comprise the event sample.

Another missing-mass distribution of interest is the neutral mass recoiling from the charged tracks (the $\pi^+ p$ system). This is shown in Fig. 5 for events which satisfy the constraint of fitting reaction (1) with a probability $>1\%$. This is shown separately for (a) events with no missing neutrals, (b) events with a single missing γ, and (c) events with a missing π^0. One notes from these distributions that the higher the missing mass, the lower is the number of detected γ's. This is simply a result of our geometric acceptance. The low-mass dipion system (with low Q-value) decays more forward in the laboratory with a greater likelihood for all γ's to enter the lead-glass hodoscope than the high-mass systems. A second feature present in the data is the presence of the expected peak at dipion masses in the f-meson region, evident in Fig. 5(c).

The data sample chosen for further analysis was com-

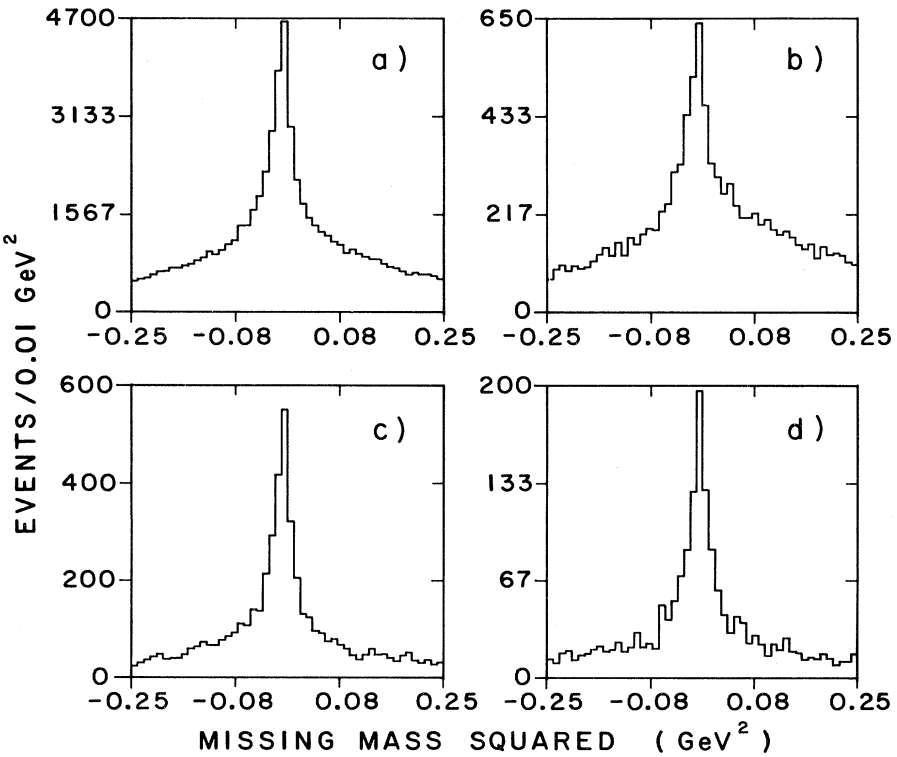

FIG. 4. Overall missing-mass-squared distributions for (a) one-, (b) two-, (c) three-, and (d) four-cluster events.

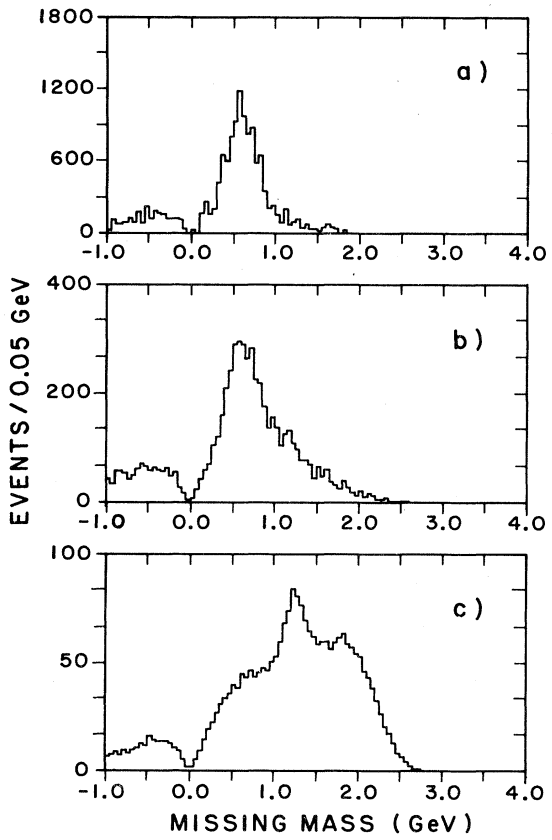

FIG. 5. Missing mass recoiling from the π^+p system for events with (a) no missing neutrals, (b) a single missing γ, and (c) a missing π^0.

posed of those events consistent with reaction (1) (with a χ^2 probability greater than 1%) which are not consistent with fitting the higher-constraint-class reaction (2). There were 36 739 such events. A large number of these events are also consistent with reaction (3), but the missing-mass distribution shown in Fig. 6 shows that this is generally an incorrect fit. This distribution of the missing mass recoiling from the hypothesized $\pi^+\pi^+\pi^0$ system shows very little evidence for a neutron signal. Monte Carlo studies also show that in fact it is very unlikely for a valid event of reaction (3) to produce two π^+ mesons with slow laboratory momentum such as the events in our sample. We

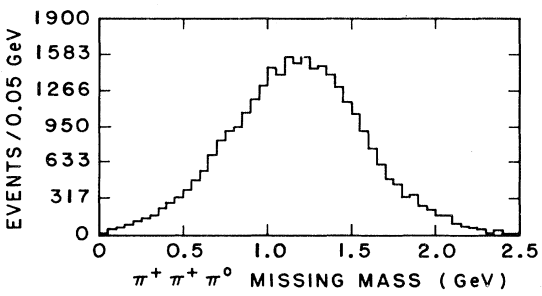

FIG. 6. Missing mass recoiling from the hypothesized $\pi^+\pi^+\pi^0$ system.

thus ignore the fits to reaction (3) in the ensuing analysis, and estimate background due to this final state to be less than 5%.

Events ambiguous by virtue of having more than one acceptable fit for reaction (1) fell into two categories. First, an event can have a charged-track ambiguity—that is, acceptable fits occur with each of the two charged tracks hypothesized as proton and π^+. The first selection criteria used for these events was based on χ^2 probability. Defining P_1 to be the probability of the more likely hypothesis and P_2 the probability of the less likely hypothesis, the more likely hypothesis was selected if $P_1 > 1.33P_2 + 0.2$. Otherwise, the hypothesis chosen for further analysis consisted of that hypothesis whose π^+-proton effective mass was closer to 1.238 GeV. (This criterion was compared with various other methods for selection based on such criteria as χ^2 probability and positive-track momentum, and we find that the results of our analysis do not depend strongly on the procedure used.) Second, an event can have a neutral-track ambiguity, that is, an ambiguity which occurs when, for example, in a three-cluster event one gets acceptable hypotheses with different permutations of the clusters for the π^0. These ambiguities were treated by using both hypotheses for analysis but weighting them in proportion to their χ^2 probability.

Further cuts on the data were carried out[20] to ensure that the data sample was as free from instrumental bias and from background as possible. These cuts included a cut on steeply dipping charged tracks, which had a detection bias in the streamer chamber; on very-high-weight events; on production vertex position; on charged-track projected momentum (corresponding to the scanning cut described above); and, for those events fitted with a missing π^0, a cut on its direction ensuring it should not have been detected by the hodoscope. The event sample consists of 26 998 events after these cuts.

In order to take into account the geometric acceptance of the apparatus in the analysis to follow, each event in the final sample was weighted inversely with the probability of its being detected. This weighting factor was determined by generating Monte Carlo events for each real event with the same momentum transfer, $\pi^0\pi^0$ effective mass, and $\pi^0\pi^0$ decay angles (Gottfried-Jackson and Trieman-Yang angles) as the real event. The Monte Carlo events were generated randomly about an axis defined by the beam direction. The π^0 decay was generated isotropically, and the generated event was then tested to determine if it would trigger the apparatus and pass the data cuts. Monte Carlo events were generated for each real event until its weight was known to better than 5%. The average weight for the data sample as a whole was 2.17. Distributions shown in the remainder of this paper are based on weighted data unless explicitly stated.

IV. GENERAL FEATURES OF THE DATA

Shown in Fig. 7 is the π^+p effective-mass spectrum for the event sample (weighted and unweighted). The dominant presence of the Δ^{++} resonance is clear. Note that the acceptance does not vary strongly with π^+p effective

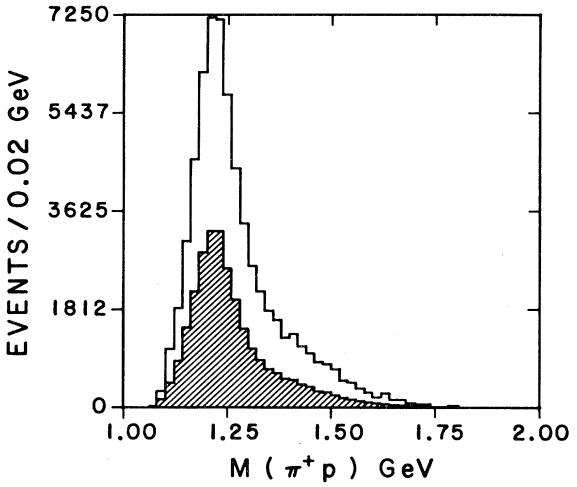

FIG. 7. The π^+p effective-mass distribution for the final data sample (weighted and unweighted).

mass. For futher analysis a cut requiring the π^+p mass to be less than 1.36 GeV was made in order to select Δ^{++} production more cleanly.

The $\pi^0\pi^0$ effective-mass distribution is shown in Fig. 8 for events with (a) no missing particles, (b) a missing γ, (c) a missing π^0, and (d) all events. In each case both weighted and unweighted distributions are shown. One notes the bias toward low effective mass if one requires no missing particles as discussed with regard to the missing-mass distributions of Fig. 5. Note also the rather smooth variation of the average weight as a function of $\pi^0\pi^0$ mass. Finally, the most prominent feature of the data is the expected production of the $f^0(1270)$. The average $\pi^0\pi^0$ mass resolution as a function of $\pi^0\pi^0$ mass is shown in Fig. 9. The error bars here indicate 1 standard deviation on the spread

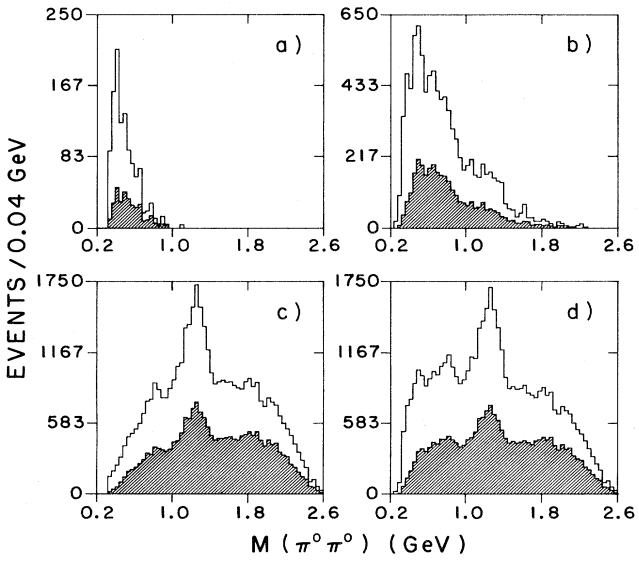

FIG. 8. The $\pi^0\pi^0$ effective-mass distribution (weighted and unweighted) for events with (a) no missing particles, (b) a missing γ, (c) a missing π^0, and (d) all events.

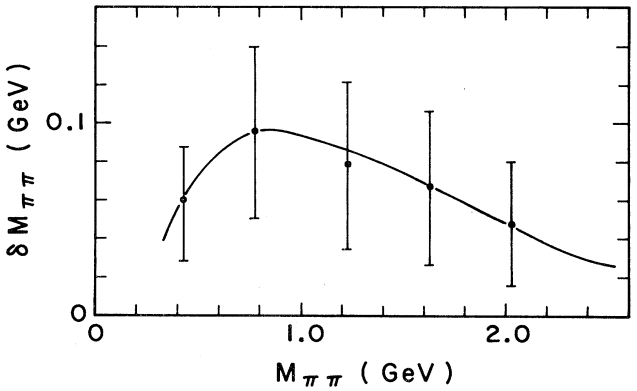

FIG. 9. The average $\pi^0\pi^0$ effective-mass error as a function of $\pi^0\pi^0$ effective mass. The error bars indicate one standard deviation on the spread of the values of the errors.

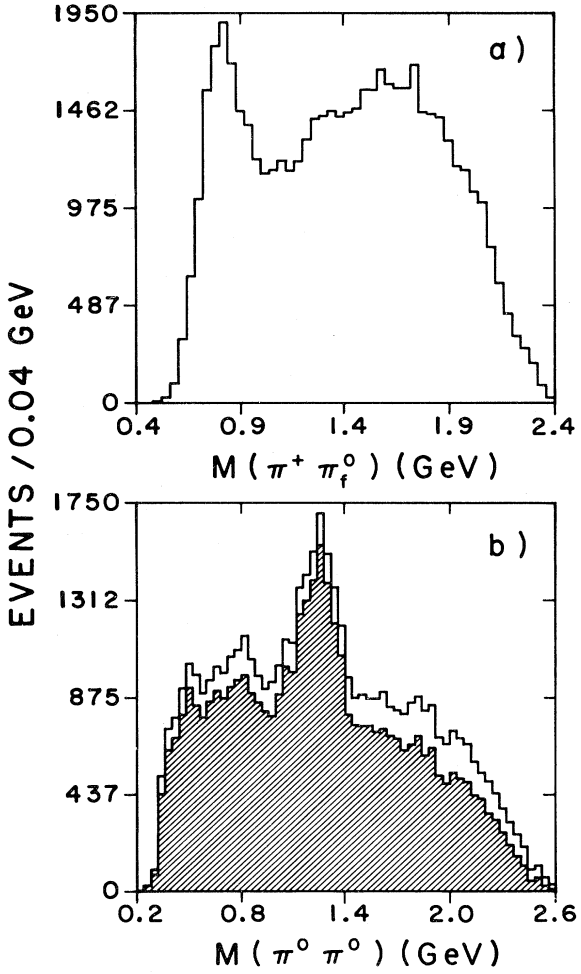

FIG. 10. (a) The $\pi^+\pi^0_f$ effective-mass distribution for all events. (The combination plotted is the one with the fastest π^+ in the laboratory.) (b) The $\pi^0\pi^0$ effective-mass distribution for events falling outside the ρ^+ cut. (The full histogram is the total $\pi^0\pi^0$ mass spectrum.)

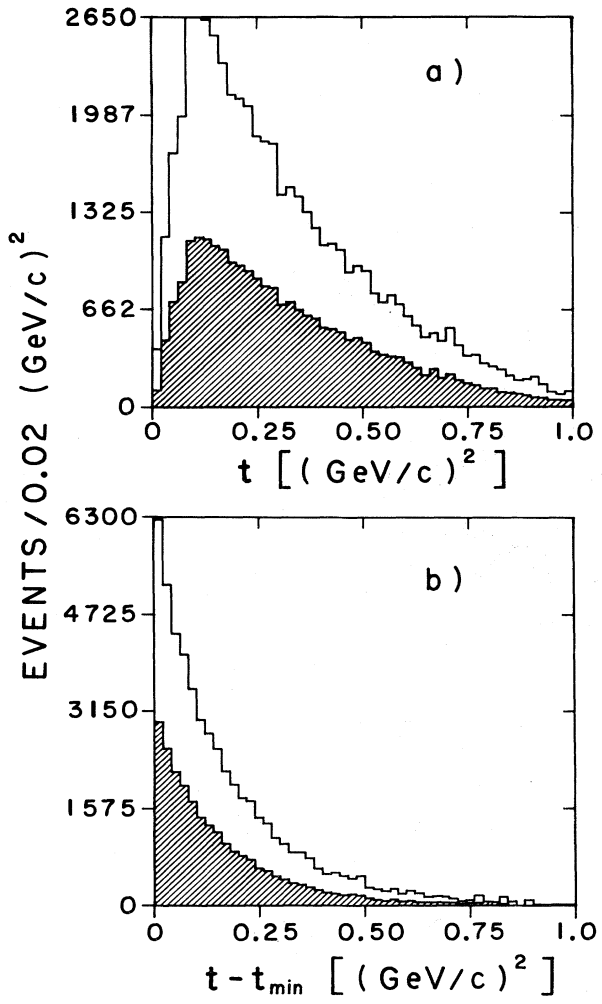

FIG. 11. (a) Distribution of the momentum transfer $|t|$ from the target proton to the $\Delta^{++}(1236)$ (weighted and unweighted). (b) Distribution of $|t-t_{\min}|$ (weighted and unweighted).

of the values of the errors to indicate the range uncertainties.

The primary purpose of this work is to study π-π scattering using the reaction $\pi^+\pi^-\to\pi^0\pi^0$ from the reaction $\pi^+p\to\Delta^{++}\pi^0\pi^0$. As such, the reaction $\pi^+p\to p\rho^+\pi^0$ can be considered a source of background. The presence of this latter reaction can be illustrated from the $\pi^+\pi^0_f$ mass distribution shown in Fig. 10(a). Here the π^0 chosen to plot is the fastest (in the laboratory), and is the combination which contains a very clear ρ^+ signal. In order to see how this background affects the analysis, the $\pi^0\pi^0$ effective-mass distribution for events which fall outside a ρ^+ cut is shown in Fig. 10(b). (The $\pi^+\pi^0_f$ mass was required to fall outside the region between 0.66 and 0.86 GeV for this histogram.) The effect is distributed rather uniformly in $\pi^0\pi^0$ effective mass. No ρ^+ cut is included in the data analysis since we assume that the extrapolation procedure itself eliminates contributions from these events in the π-π scattering analysis.

The momentum transfer, $|t|$, from the target proton to the $\Delta^{++}(1236)$ is shown in Fig. 11(a). Figure 11(b) shows the distributions of $|t-t_{\min}|$, where $|t_{\min}|$ is the lowest value of t allowed for the given $\pi^0\pi^0$ and π^+p masses in the event. These distributions, shown weighted and unweighted, are sharply peaked at low values as expected for one-pion exchange (OPE). The acceptance does not depend strongly on $|t|$. The Chew-Low plot of Fig. 12 shows the variation of $|t|$ with $\pi^0\pi^0$ mass. Note that, because of the variation of π^+p mass across the $\Delta^{++}(1236)$, the lower boundary of the Chew-Low plot is not uniquely defined.

In order to show the acceptance of our system in the important π-π scattering angles in the Gottfried-Jackson system, the weighted and unweighted distributions in $\cos\theta_J$ and ϕ_J are shown in Figs. 13 and 14, respectively, for various $\pi^0\pi^0$ masses. These distributions show that the acceptance slowly decreases, especially in the region near $|\cos\theta|=0$, as the $\pi^0\pi^0$ mass gets larger. The azimuthal acceptance on the other hand is quite uniform. The effect of this acceptance on our analysis will be discussed below.

V. $\pi^+\pi^-\to\pi^0\pi^0$ SCATTERING AMPLITUDE ANALYSIS

A. Extrapolation to the pion pole

The amplitude analysis was made with the assumption of dominance of one-pion exchange. We extract the on-shell $\pi^+\pi^-\to\pi^0\pi^0$ amplitude from the data using the expression

$$|T|^2=C\frac{q}{M_{\pi\pi}{}^2}(t+\mu^2)^2\frac{d^3N}{dt\,dM_{\pi\pi}dM_\Delta}\frac{dM_\Delta}{M_\Delta{}^2Q\sigma(\pi^+p)} \tag{4}$$

which describes the π-π scattering amplitude at the pole ($t=-\mu^2$). Here q and Q are the center-of-mass momenta in the $\pi^0\pi^0$ and the π^+p rest systems, respectively, $\sigma(\pi^+p)$ is the elastic π^+p cross section at the energy M_Δ, and C is a constant for a fixed beam energy. In the analysis the right-hand side of Eq. (4) was evaluated event by event as a function of $M_{\pi\pi}$ and t, by summing over M_Δ; each event is corrected by the detection probability discussed in the previous section. The value of $|T|^2$ is then obtained by extrapolating the experimental values to $t=-\mu^2$.

The extrapolation of $|T|^2$ from experimental data using Eq. (4) can be done in several ways. If the data for a given $M_{\pi\pi}$ are summed over the entire π-π scattering angular distribution ($\cos\theta_J$ and ϕ_J), then the $|T|^2$ value corresponds to the total elastic off-shell $\pi^+\pi^-\to\pi^0\pi^0$ cross section for that $M_{\pi\pi}$; the extrapolation of these values to the pion pole would then yield the total elastic on-shell $\pi^+\pi^-\to\pi^0\pi^0$ cross section. In this paper, we are interested in determining the amplitudes for each partial wave; to achieve this, each event is weighted by the Legendre polynomial $Y_L^m(\cos\theta,\phi)$ and the moments of the angular distributions are obtained by summing over all events. These off-shell moments are shown unshaded in Fig. 15 as a function of $M_{\pi\pi}$ (summed over all t) for $M_{\pi\pi}<1.5$ GeV. The moments $\langle Y_L^m\rangle$ with $m\neq 0$ are negligible and are not

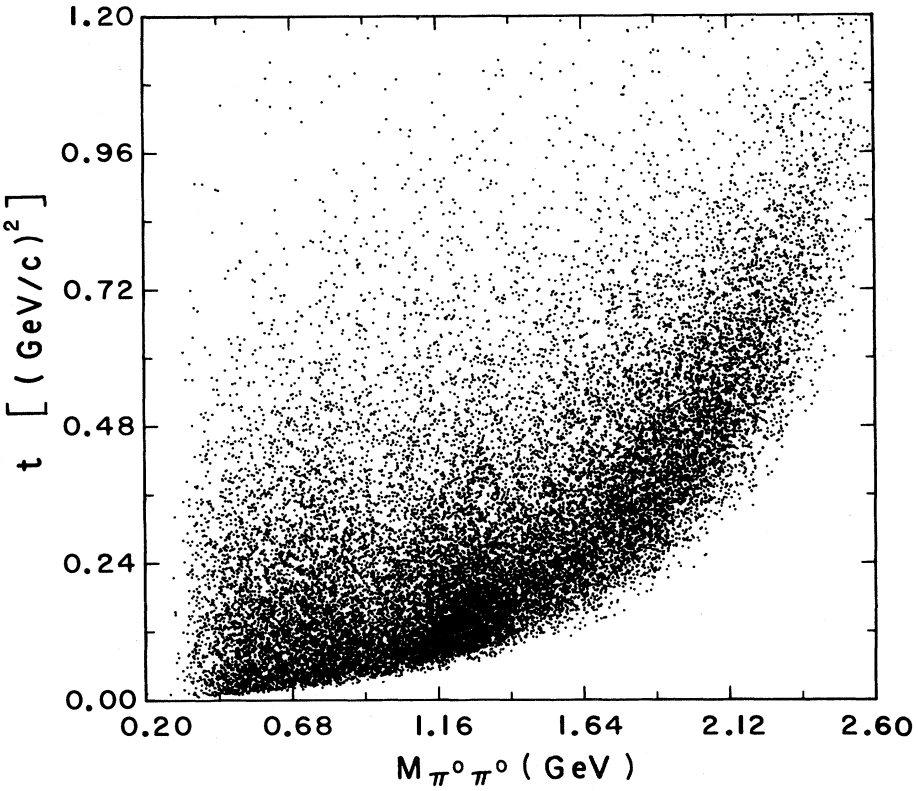

FIG. 12. Scatter plot (Chew-Low plot) of the momentum transfer from the target proton to the $\Delta^{++}(1236)$ versus the $\pi^0\pi^0$ effective mass.

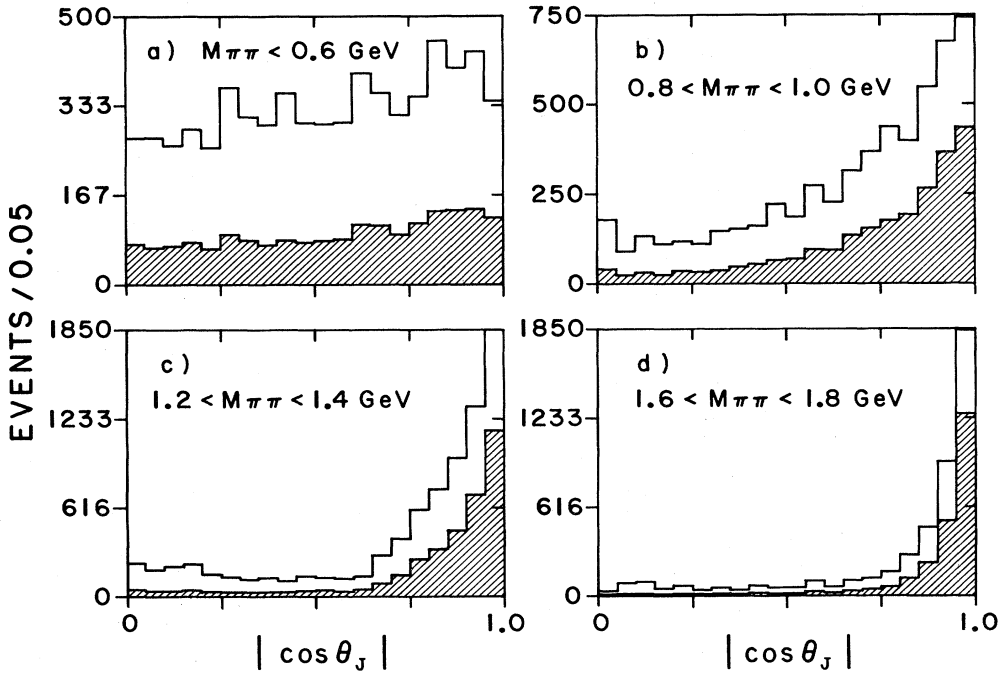

FIG. 13. Unweighted (shaded) and weighted distributions of $\cos\theta_J$ where θ_J is the scattering angle in the t channel for π-π scattering for the π-π mass intervals indicated.

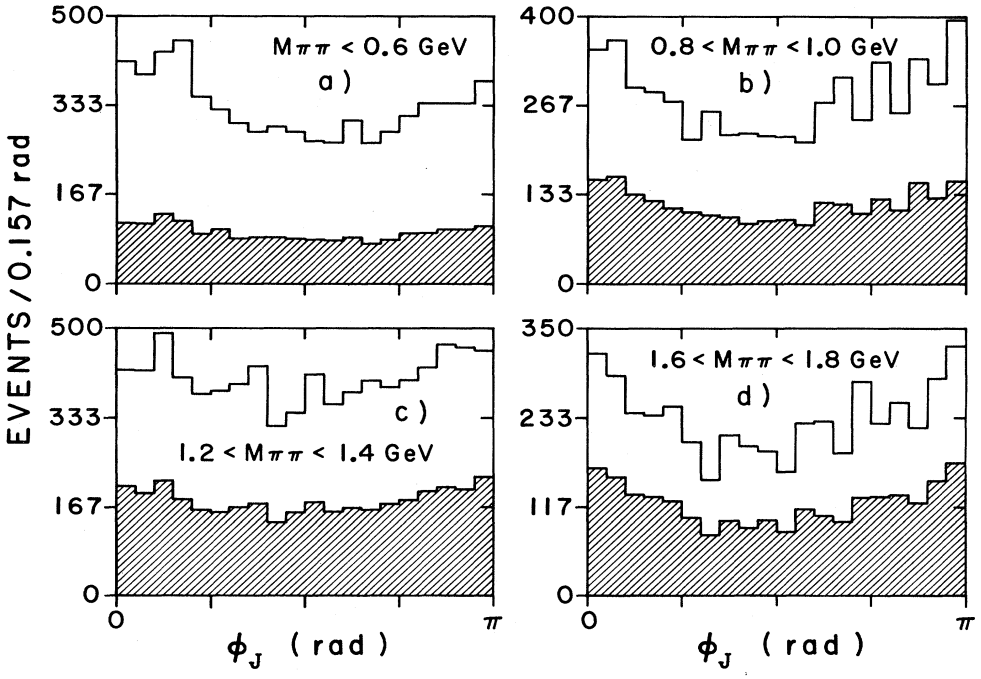

FIG. 14. Unweighted (shaded) and weighted distributions of the azimuthal angle ϕ_J for the mass intervals indicated.

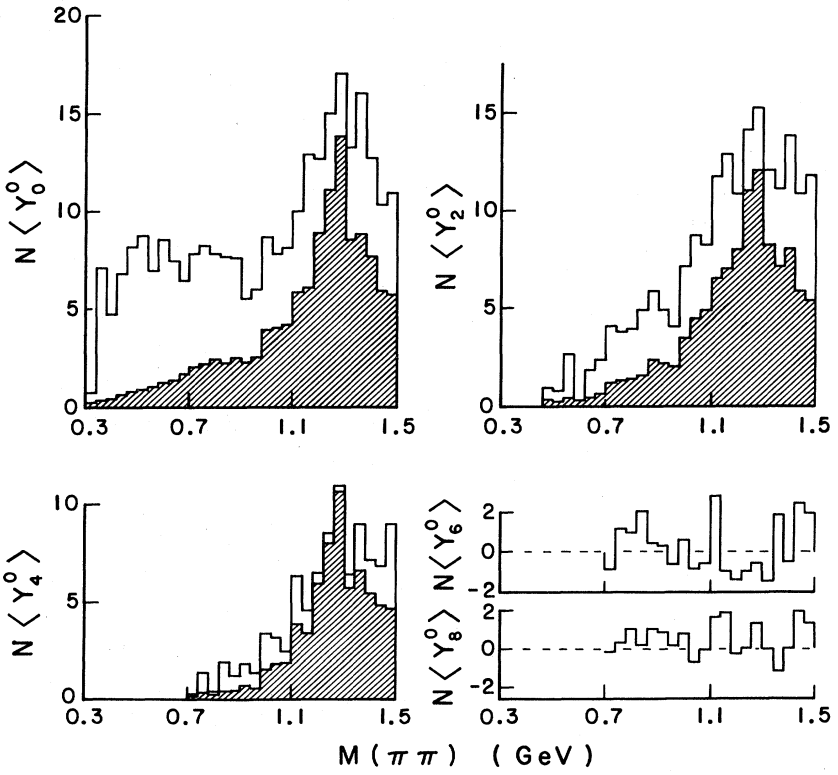

FIG. 15. Distributions of the unnormalized moments $N\langle Y_L^0 \rangle$ (events/0.04 GeV) as a function of $\pi^0\pi^0$ mass. Shaded distributions are the extrapolated moments.

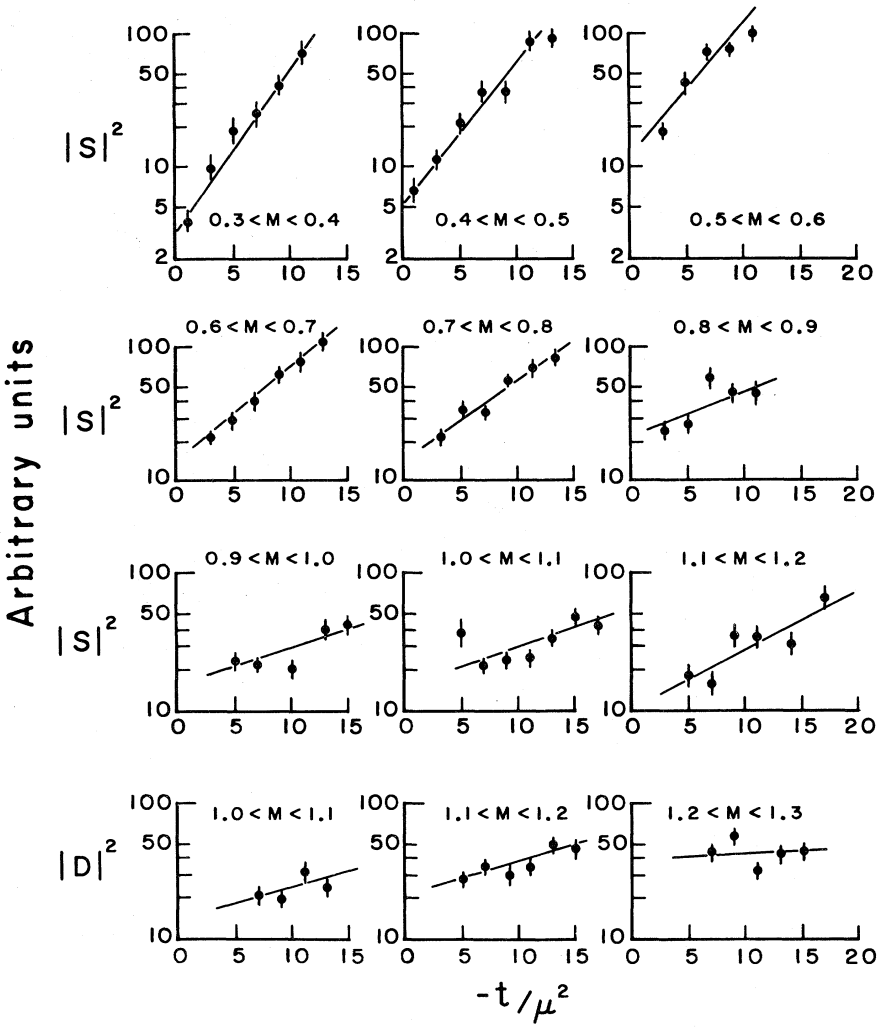

FIG. 16. $|S|^2$ and $|D|^2$ as a function of t for the various $\pi^0\pi^0$ mass intervals indicated. The straight lines are fits to the data used to obtain the extrapolated amplitudes.

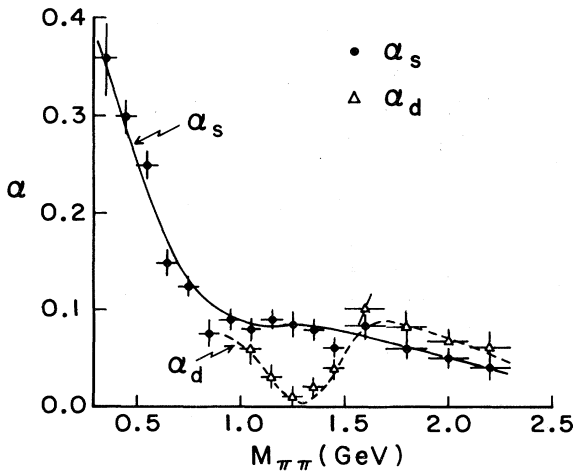

FIG. 17. The extrapolation coefficients (see text) α_S and α_D as a function of $M_{\pi\pi}$. The smooth curves are intended to guide the eye.

shown. The $m=0$ moments for $L>8$ are also consistent with zero and are not shown. We find that, for $M_{\pi\pi}<1.7$ GeV, only the moments up to $L=4$ are significant, and for $M_{\pi\pi}>1.7$ GeV the moments up to $L=8$ are important; thus, it is sufficient to consider only S and D waves for the low-mass region and include G waves for $M_{\pi\pi}>1.7$ GeV.

The standard procedure used to determine the scattering amplitudes is to extrapolate the significant off-shell moments to the pion pole to evaluate the on-shell moments. The partial-wave amplitudes are then obtained from these on-shell amplitudes. We have, however, followed a different procedure. We note that the off-shell partial-wave intensities may be obtained directly from the off-shell moments by

$$|S|^2=\langle Y_0^0\rangle-\tfrac{7}{6}\langle Y_4^0\rangle$$
$$=\frac{1}{N}\sum[Y_0^0(\theta_i)-\tfrac{7}{6}Y_4^0(\theta_i)] \quad (5)$$

TABLE I. On-shell moments as a function of $M_{\pi\pi}$.

$M_{\pi\pi}$ (GeV)	$\langle Y_0^0 \rangle$	$\langle Y_2^0 \rangle$	$\langle Y_4^0 \rangle$	$\langle Y_6^0 \rangle$	$\langle Y_8^0 \rangle$
0.30–0.34	0.03±0.02				
0.34–0.38	0.16±0.04				
0.38–0.42	0.09±0.02				
0.42–0.46	0.17±0.03				
0.46–0.50	0.19±0.03				
0.50–0.54	0.29±0.04				
0.54–0.58	0.28±0.04				
0.58–0.62	0.45±0.06				
0.62–0.66	0.62±0.07	0.08±0.07	0.06±0.06		
0.66–0.70	0.75±0.09	0.16±0.09	−0.002±0.05		
0.70–0.74	0.89±0.06	0.35±0.07	0.03±0.05		
0.74–0.78	0.90±0.06	0.43±0.07	0.06±0.06		
0.78–0.82	0.97±0.06	0.46±0.07	0.03±0.07		
0.82–0.86	0.91±0.06	0.49±0.06	0.07±0.06		
0.86–0.90	1.00±0.06	0.76±0.08	0.12±0.06		
0.90–0.94	0.87±0.06	0.63±0.08	0.24±0.07		
0.94–0.98	0.88±0.07	0.65±0.08	0.25±0.07		
0.98–1.02	1.27±0.10	1.04±0.12	0.44±0.10		
1.02–1.06	1.38±0.10	1.50±0.13	0.60±0.11		
1.06–1.10	1.30±0.09	1.54±0.13	0.52±0.09		
1.10–1.14	1.90±0.13	2.01±0.16	1.28±0.13		
1.14–1.18	1.89±0.12	2.18±0.15	1.12±0.12		
1.18–1.22	2.50±0.15	2.32±0.19	1.59±0.16		
1.22–1.26	3.78±0.25	3.49±0.29	2.80±0.25		
1.26–1.30	4.24±0.28	3.77±0.32	3.15±0.27		
1.30–1.34	3.33±0.27	2.64±0.31	2.43±0.28		
1.34–1.38	2.83±0.23	2.58±0.25	2.30±0.23		
1.38–1.42	1.17±0.13	1.18±0.17	0.80±0.13		
1.42–1.46	0.40±0.04	0.38±0.05	0.14±0.04		
1.46–1.50	0.44±0.05	0.41±0.06	0.30±0.05		
1.50–1.58	0.29±0.02	0.39±0.03	0.30±0.03	0.11±0.03	0.06±0.02
1.58–1.66	0.30±0.02	0.44±0.04	0.30±0.03	0.16±0.03	0.05±0.02
1.66–1.74	0.99±0.07	1.42±0.12	0.80±0.13	0.38±0.11	0.07±0.08
1.74–1.82	1.39±0.11	2.36±0.19	1.73±0.19	0.76±0.14	0.06±0.09
1.82–1.90	1.32±0.10	2.00±0.17	1.33±0.16	0.50±0.14	−0.11±0.09
1.90–1.98	1.20–0.10	2.02±0.18	1.41±0.18	0.55±0.13	0.12±0.06
1.98–2.06	0.68±0.07	1.11±0.11	0.93±0.13	0.50±0.09	0.22±0.09
2.06–2.14	0.45±0.07	0.72±0.09	0.64±0.12	0.28±0.07	0.11±0.06
2.14–2.22	0.58±0.07	1.00±0.12	0.73±0.12	0.30±0.08	0.06±0.06
2.22–2.30	0.27±0.07	0.38±0.08	0.26±0.08	0.08±0.06	0.04±0.06

and

$$|D|^2=\tfrac{7}{6}\langle Y_4^0\rangle=\frac{7}{6N}\sum Y_4^0(\theta_i) \tag{6}$$

for the mass region $M_{\pi\pi}<1.7$ GeV. For fixed values of $M_{\pi\pi}$ and t each event is weighted by $[Y_0^0-\frac{7}{6}Y_4^0]$ and $\frac{7}{6}Y_4^0$ and all events are summed using the right-hand sides of Eqs. (5) and (6) to obtain $|S|^2$ and $|D|^2$, respectively. Figure 16 shows the dependence of $|S|^2$ and $|D^2$ on t for various mass intervals. The off-shell partial-wave intensities $|L|^2$ are dependent on t; this t dependence could be parametrized by means of the expression

$$|L|^2=|L_0|^2\exp[\alpha_L(t+\mu^2)]\equiv F^2(\alpha_L,t)\,|L_0|^2\,,$$

where $|L_0|^2$ is the intensity at the pion pole (on-shell intensity). The solid lines in Fig. 16 show the fits to the data. In Fig. 17, we show the coefficients α_S and α_D for S and D waves as a function of $M_{\pi\pi}$. The curve shown in the figure is hand drawn to guide the eye. Note that a value of $\alpha_L=0$ would be expected if there were no absorption, background, or off-shell effects in the π-π amplitudes. These effects are indeed small for the D wave in the f region; in the other mass regions, these effects are not negligible and influence the S-wave amplitudes more strongly than the D wave for the mass region $M_{\pi\pi}<1.7$ GeV; above this mass region all waves (including the G wave, not shown) are affected about equally.

For our data analysis, we are only interested in the coefficients α_L from the extrapolation. Once these α_L's are determined, we reuse the experimental data to obtain on-shell partial wave intensities by weighting each event by the off-shell correction factor. For $M_{\pi\pi}<1.7$ GeV, where only S and D waves are present, we obtain on-shell ampli-

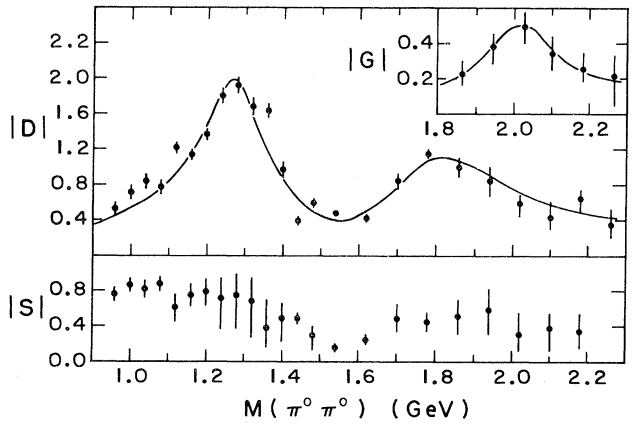

FIG. 18. Magnitudes of the S-, D-, and G-wave amplitudes for $\pi^+\pi^-\to\pi^0\pi^0$ scattering, The smooth curves are Breit-Wigner fits to the data described in the text.

tudes from

$$|D|^2=\tfrac{7}{6}\sum Y_4^0(\theta_i)F^{-2}(\alpha_{D_i},t_i)\ ,$$

$$|S|^2=\sum[Y_0^0-\tfrac{7}{6}Y_4^0(\theta_i)]F^{-2}(\alpha_{S_i},t_i)\ ,$$

and

$$2S^*D=\sum[Y_2^0(\theta_i)-\frac{\sqrt{5}}{3}Y_4^0(\theta_i)]F^{-1}(\alpha_{D_i},t_i)F^{-1}(\alpha_{S_i},t_i)\ .$$

Using these amplitudes, we calculate the extrapolated (on-shell) moments using the relations

$$\langle Y_0^0\rangle=|S|^2+|D|^2\ ,$$

$$\langle Y_2^0\rangle=2S^*D+0.639|D|^2\ ,$$

and

$$\langle Y_4^0\rangle=0.857|D|^2\ .$$

The effect of this weighting of the data by $F^2(\alpha,t)$ can be seen in the cross-hatched region of Fig. 15 which shows the extrapolated moments.

For $M_{\pi\pi}>1.7$ GeV, the off-shell (on-shell) moments are related to off-shell (on-shell) amplitudes by the relations

$$\langle Y_0^0\rangle=|S|^2+|D|^2+|G|^2\ ,$$

$$\langle Y_2^0\rangle=2S^*D+0.639|D|^2+1.714G^*D+0.581|G|^2\ ,$$

$$\langle Y_4^0\rangle=0.857|D|^2+2S^*G+1.162D^*G+0.486|G|^2\ ,$$

$$\langle Y_6^0\rangle=1.691D^*G+0.504|G|^2\ ,$$

and

$$\langle Y_8^0\rangle=0.831|G|^2\ .$$

Similarly to the lower-mass data, the off-shell values of $|S|^2$, $|D|^2$, $|G|^2$, S^*D, S^*G, and D^*G were determined from the off-shell moments and were extrapolated to the pion pole. In this mass region we find that α is independent of L (i.e., $\alpha_S=\alpha_D=\alpha_G$). The on-shell moments were then obtained using these extrapolated values.

The on-shell amplitudes were normalized using the well-known value $|D|^2=5[(1+\eta_D)/2]^2$ with $\eta_D=0.67$ in the f^0 mass region. The on-shell moments with this normalization are tabulated in Table I and the values of $|S|$, $|D|$, and $|G|$ as a function of $M_{\pi\pi}$ are plotted in Fig. 18. Note that the resolution shown in Fig. 9 precludes us from observing sharp effects due to the S^* near 1.0 GeV.

We note that, in the procedure described above, the on-shell partial-wave amplitudes are obtained by directly extrapolating the corresponding amplitudes instead of obtaining these amplitudes via the standard procedure of extrapolation of the off-shell moments. It is obvious that if all the partial waves are affected equally by absorption and other off-shell effects, then either procedure will yield the same results. However, in the mass region from 1.0 to 1.5 GeV, the S- and D-wave amplitudes are affected differently (see Fig. 17), and the two methods yield different values of $|S|^2$ and $|D|^2$. In fact, the moment extrapolation method would overestimate $|S|^2$ relative to $|D|^2$ since the S wave shows more "absorption."

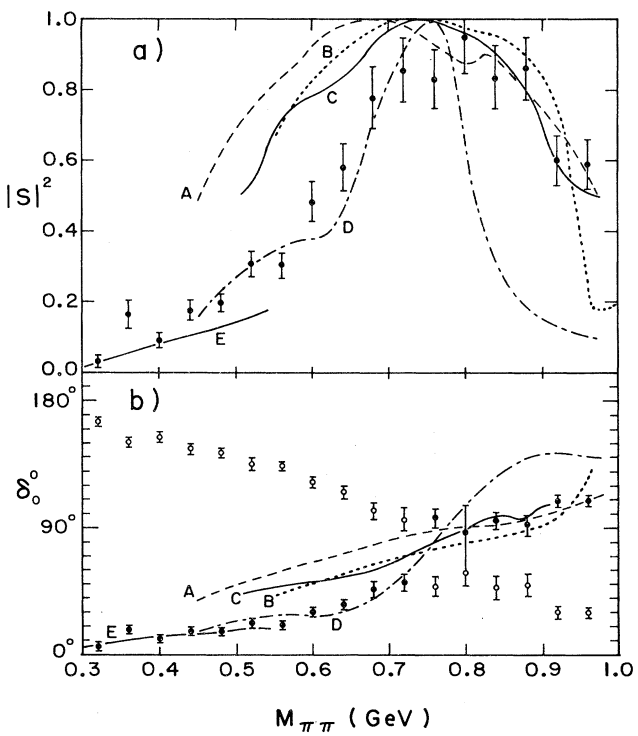

FIG. 19. (a) Extrapolated S-wave intensity as a function of $\pi^0\pi^0$ mass. Shown as smooth curves are predictions based on $\pi^+\pi^-\to\pi^+\pi^-$ scattering (A and D from Ref. 3, B from Ref. 5, and C from Ref. 7) and on current algebra and PCAC (curve E). (b) $I=0$, S-wave phase shifts determined in our experiment. The two ambiguous solutions are shown as open and closed circles. The curves are as in (a).

B. The elastic region

The values of $|S|^2$ from threshold to 0.96 GeV are plotted in Fig. 19(a). The S-wave intensity $|S|^2=|a_0-a_2|^2$ is related to the phase shifts by $a_I=\exp(i\delta_I)\sin\delta_I$. For the $I=2$ S-wave phase shift we use $\delta_0^2=-q/(1.1+0.884\,07q^2)$, with q in GeV/c and δ_0^2 in radians, which is a good parametrization of the available data.[28] The uncertainty in δ_0^2 is small compared to the statistical errors in our data and does not affect our results. Also shown in Fig. 19(a) as curves A–D are predictions based on analyses of $\pi^+\pi^-\to\pi^+\pi^-$ data. Curves B and C are most representative of the currently accepted[29] S-wave amplitude. Our data are in clear agreement with A, B, and C above 0.84 GeV. They are, however, inconsistent with these predictions below 0.68 GeV. Here our data clearly require a solution of the type represented by curve D. This result is in disagreement with conclusions[3] drawn from previous[12] unextrapolated $\pi^0\pi^0$ data which appeared to favor the currently accepted solution in this entire mass region. It is also in disagreement with the extrapolated $n\pi^0\pi^0$ data[17] at 2.01 GeV. (The extrapolation in that final state is considerably more difficult than in the $\Delta^{++}\pi^0\pi^0$ final state because of the vanishing of the physical amplitude at $t=0$.) It is however consistent with the $n\pi^0\pi^0$ data of Skuja *et al.*[13] whose results we now confirm.

In Fig. 19(b) are shown the $I=0$ S-wave phase shifts as determined directly from our data using the $I=2$ phase-shift parametrization described above. There is a discrete ambiguity in that two values of δ_0^0 lead to the same value of $|S|^2$ when combining an $I=0$ amplitude with an $I=2$ amplitude. As pointed out by Skuja *et al.*,[13] the only type of solution for $\pi^+\pi^-\to\pi^0\pi^0$ consistent with the $\pi^+\pi^-\to\pi^+\pi^-$ data is the so-called "down-down" solution, represented by curve D below 0.68 GeV and by the standard solution above 0.84 GeV. This leads to a rather rapid phase variation at approximately 0.75 GeV and a phase shift which goes through 90° at about 0.80 GeV.

Our data near threshold confirm the predictions[1,30] based on PCAC (partial conservation of axial-vector current) and current algebra. These predictions, which had been previously thought not to be valid,[17] are shown by the curve E in Fig. 19.

The phase behavior is not well represented by a narrow Breit-Wigner resonance at 700 MeV. The phase variation is rapid below resonance ("narrow" behavior) and rather slow above resonance ("broad" behavior). Thus, if a narrow $\epsilon(700)$ is assumed, one must postulate the existence of a background, such as the S^*, which becomes important above resonance.

The phase difference δ_0^2-δ_0^0 at the mass of the neutral K meson is related to the CP violation parameters in K decay[31] and is predicted to be $-40.6°\pm3°$ using current values for δ_0^2-δ_0^0. We obtain δ_0^2-$\delta_0^0=-29.2°\pm3°$ from our data. The difference between our value and the predicted value is probably within systematic uncertainties associated with the phase-shift measurements and with electromagnetic effects in K decay. Our solution is in significantly better agreement than the result based on the standard solution δ_0^2-$\delta_0^0=-58°\pm3°$.

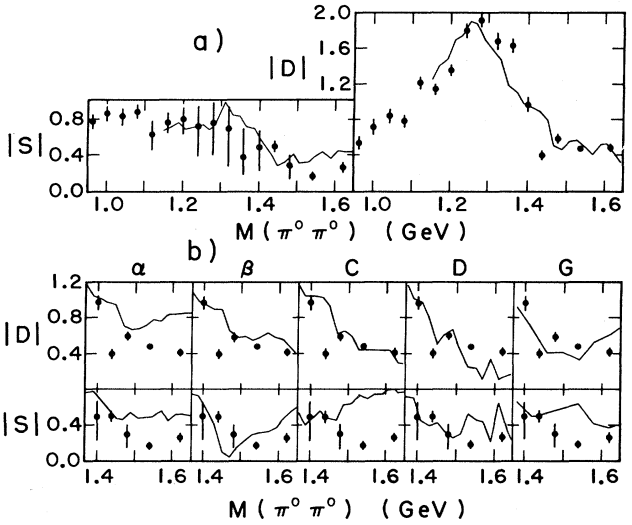

FIG. 20. (a) Magnitudes of the S- and D-wave amplitudes for $\pi^+\pi^-\to\pi^0\pi^0$ scattering. The connected lines represent solution β' from Ref. 9. (b) Comparison of the amplitudes from this experiment (data points with error bars) with solutions α and β from Ref. 9; solutions C and D from Ref. 7; and solution G from Ref. 10.

C. $1.0<M_{\pi\pi}<1.7$ GeV

Since $\langle Y_6^0\rangle$ and $\langle Y_8^0\rangle$ are small below 1.7 GeV, the amplitudes in this region, shown in Fig. 20(a), were obtained assuming $|G|=0$. The most apparent features of these amplitudes are the dominant $f^\circ(1270)$ in the D wave and the dramatic decrease in $|S|$ which reaches a minimum at about 1.54 GeV.

The π-π scattering amplitudes determined from previous $\pi^+\pi^-\to\pi^+\pi^-$ experiments have a fourfold ambiguity in this energy region. The four ambiguous solutions have been denoted as A, B, C, and D. Another analysis[9] yielded solutions called α, β, and β' which are variations of A and B which arise after imposing analyticity on them. A more recent experiment[10] favors yet another solution called G. In order to compare our results with

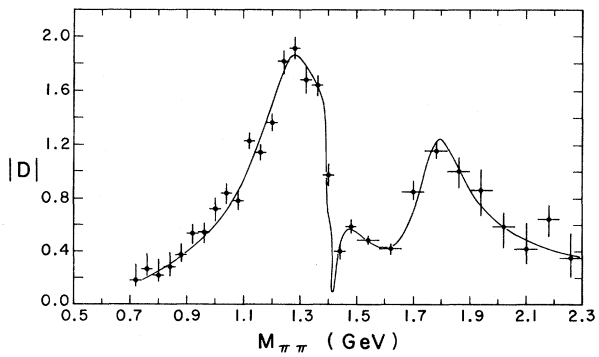

FIG. 21. Magnitude of the D-wave amplitude as a function of $M_{\pi\pi}$. The smooth curve is a three-Breit-Wigner-resonance fit discussed in the text.

these amplitudes it is necessary to take into account the $I=2$ contributions which enter differently in the $\pi^+\pi^-$ final state and the $\pi^0\pi^0$ final state. We have taken the $\pi^+\pi^-\to\pi^+\pi^-$ solutions from Refs. 7–10 and obtained the predicted $\pi^+\pi^-\to\pi^0\pi^0$ amplitudes again assuming $I=2$ S- and D-wave phase shifts consistent with those measured by Hoogland *et al.*[28] The resulting predictions are shown as the connected line segments in Figs. 20(a) and 20(b). Solution β' shown in Fig. 20(a) is in best agreement with the $|S|$ and $|D|$ determined from our data. We confirm that solutions C and D are incompatible with the $\pi^0\pi^0$ data. Solution α is clearly ruled out by the data, predicting much too large S and D waves above 1.45 GeV. Solution G of Corden *et al.*[10] is not a good representation of our data. Finally, solution β shown in Fig. 20(b) is only slightly poorer than solution β', and when one takes into account the uncertainty in the $I=2$ amplitudes, the discrimination between these solutions is even less. We conclude that the B-type variants β and β' are the best fits to the data. Thus the $J^{PC}=2^{++}$ state at 1.55 GeV of solution A is ruled out, and we conclude that the π-π coupling of the $\rho'(1600)$, characteristic of solution B, is significant. These conclusions agree with those of Becker *et al.*[11] who find a unique solution in a polarized target experiment.

We conclude this section with the observation that the two Breit-Wigner fit of Fig. 18 (discussed in detail in the next section) is not a particularly good fit in the region around 1.4 GeV. We have as an exercise carried out a three Breit-Wigner fit to the data and note that the χ^2 for the fit decreases from 136 for 24 degrees of freedom to 36 for 20 degrees of freedom if a third (narrow) resonance at 1.4 GeV is present which is 180° out of phase with the $f^\circ(1270)$. Although we would not claim existence of this state on the basis of this single observation, we show the fit in Fig. 21 to document the effect. Should other experiments corroborate the observation, the result would be most interesting.

D. $1.7 < M_{\pi\pi} < 2.3$ GeV

Above 1.66 GeV, two complications arise. First, the $\langle Y_6^0 \rangle$ and $\langle Y_8^0 \rangle$ moments are no longer negligible, and G waves must be included. Second, the acceptance begins to vanish for π-π scattering near 90°. Hence we only fit the region $1.82 < M_{\pi\pi} < 1.98$ GeV for $|\cos\theta| > 0.1$, the region $1.98 < M_{\pi\pi} < 2.06$ GeV for $|\cos\theta| > 0.2$, and the region $M_{\pi\pi} > 2.06$ GeV for $|\cos\theta| > 0.3$. The stability of the resulting moments has been checked by varying these cuts widely, and they are sensitive to the location of the cut in only one mass bin (centered at 2.02 GeV).

The G-wave amplitude above 1.82 GeV, shown as the inset of Fig. 18, peaks in the region of the $h^0(2040)$ meson, and we have fitted the data with the G-wave Breit-Wigner form shown. The parameters thus obtained are shown in Table II. These parameters are consistent[29] with those of the $h^0(2040)$, lending confidence to our analysis at high mass.

The S and D waves above 1.66 GeV were then recalculated constraining the G wave to the fitted h-meson parameters. These are shown in Fig. 18. A second ambiguous solution is now possible, and both solutions were found using the method of Barrelet zeroes. The two solutions were very close to one another (due to the smallness of the G wave) and are within the 1-standard-deviation error bars shown in Fig. 18. We note a very significant D-wave peak at around 1.8 GeV which has not been observed in other π-π amplitude analyses. Although we cannot rule out $I=2$ for the state, we henceforth refer to it as the $f'(1800)$. Such an effect has been recently reported in K^+K^- data,[32] and our observation may be another decay mode. The smooth curve shown in Fig. 18 is a two Breit-Wigner fit to the D-wave amplitude, and the parameters of that fit are shown in Table II.

It is interesting to speculate on the nature of the $f'(1800)$ observed in the data. Since the members of the $J^P=2^+$ q-$\bar{q}$ nonet are very well established, we must assume the new state is "unusual"; it might be a $2q$-$2\bar{q}$ state, a glueball, or a q-$\bar{q}$ radial excitation. If it were a $2q$-$2\bar{q}$ state, many other states including exotics, as yet unobserved, should exist[33,34] in this energy regime. Furthermore, the observed state is somewhat higher in mass than expected for the states which couple strongly to π-π. The glueball alternative is viable since the low-lying glueball states are predicted[35] to include a 2^+ state, although again the observed mass is higher than expected and the width is greater than expected in some models. Also, such a strong coupling to the π-π state would be somewhat surprising in light of the many other energetically allowed states such as $\eta\eta$ and $\eta\pi\pi$ which are believed to couple strongly to glue. The most likely possibility is that we are observing a radial excitation of the $f^\circ(1270)$ since various calculations[36] estimate the excitation energy of such a state to be of the order of 600 MeV and the coupling to π-π is expected.

E. Phase-shift analysis from 1.0 to 1.5 GeV

In order to determine the S-wave phase shifts in the region near the f meson, we have used the D-wave Breit-Wigner fit shown in Fig. 18 to determine the absolute phase, the S-D phase difference determined from the fit of the amplitudes to the moments, and the $I=2$ phase shifts used in the amplitude analysis. The resulting phase shifts δ and absorption parameters η are shown in Fig. 22. There are two solutions for each mass bin which are shown as open and closed circles. Below 1.1 GeV and above 1.4 GeV only one solution is shown since the second is inconsistent with unitarity. In addition, above 1.32 GeV, one solution for δ is plotted twice, differing by 180 degrees, to be used in the energy-dependent analysis discussed below. (Recall that phase shifts are determined only modulo π.)

The errors in the values of δ and η shown in Fig. 22 are

TABLE II. Parameters of the Breit-Wigner fits to the D- and G-wave amplitudes shown in Fig. 18.

J^P	2^+	2^+	4^+
Mass (GeV)	1.280 ± 0.004	1.799 ± 0.015	2.015 ± 0.028
Width (GeV)	0.152 ± 0.009	$0.280^{+0.042}_{-0.035}$	$0.816^{+0.103}_{-0.058}$
Elasticity	0.83 (fixed)	0.44 ± 0.03	0.16 ± 0.03

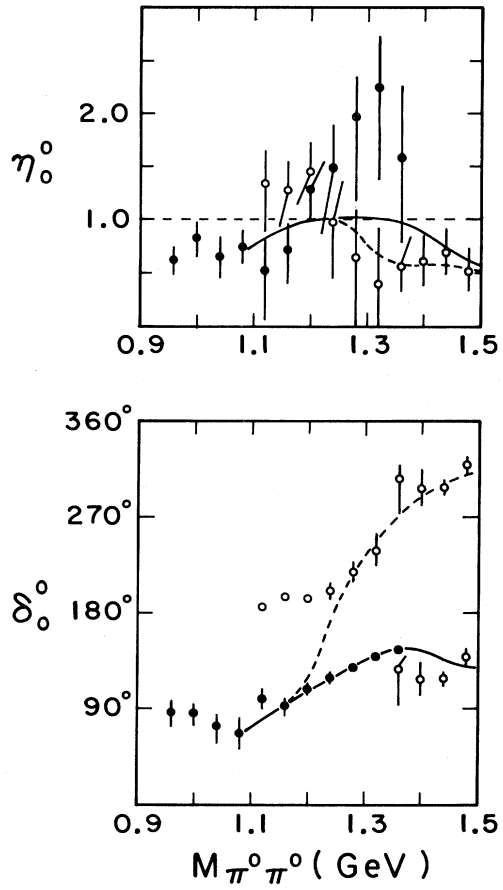

FIG. 22. $I=0$ S-wave phase shifts and absorption parameters as a function of π-π mass as determined from the data. The smooth hand-drawn curves represent the two possible types of energy-dependent solutions consistent with the data.

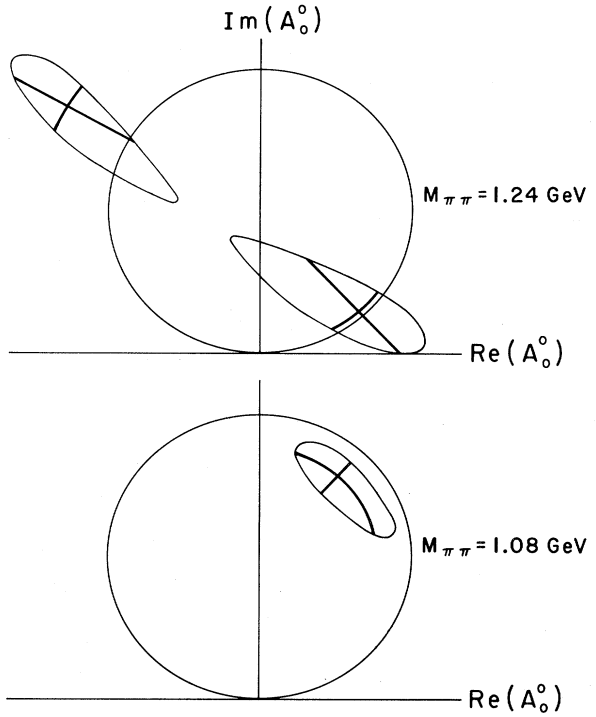

FIG. 23. One-standard-deviation contours in the Argand diagram for the phase-shift solutions found at 1.08 and 1.24 GeV.

the diagonal errors. To illustrate the correlation in the errors, we show in Fig. 23 the 1-standard-deviation-error contours for the two mass bins at 1.08 and 1.24 GeV on the Argand diagrams. Note that the correlations are such that in one case (1.08 GeV) the diagonal errors well represent the range of possible values of the parameters, while in the second case, the parameters can take on a wider range of values than those suggested by the diagonal errors. This latter case occurs for the data points between about 1.24 and 1.36 GeV, and thus the results in this region are somewhat less certain than suggested by Fig. 22.

The energy dependence of the phase shifts would seem to permit two types of solutions indicated qualitatively by the solid and dashed curves of Fig. 22. The solid curve (which we call solution I) shows a solution in which the phase shift slowly rises by about 70° in the mass range from 1.08 to 1.36 GeV and is quite elastic in this region. The amplitude then becomes slightly inelastic with an almost constant phase shift. The dashed curve (solution II) is a solution which has a very rapid phase variation in the region around 1.24 GeV. The two types of solutions are

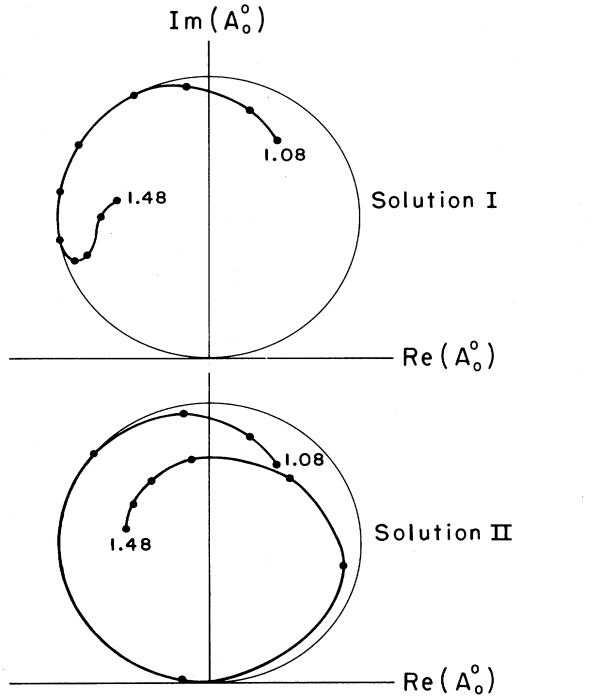

FIG. 24. Argand diagram of the $I=0$ S-wave π-π scattering amplitudes for the two types of solutions shown in Fig. 3. The data points shown are at intervals of 40 MeV.

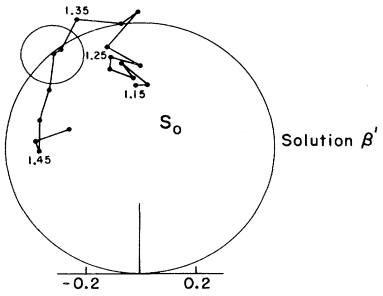

FIG. 25. Argand diagram of solution β' of Ref. 9.

shown on the Argand diagram of Fig. 24. Although solution II (with the rapid phase variation) is slightly preferred on a χ^2 basis because the absorption parameter for solution I becomes somewhat greater than unity for several of the points between 1.2 and 1.4 GeV, there has been no evidence for such a rapid phase variation in previous experiments. In fact our solution I is quite compatible with solution β' as can be seen from Fig. 25, which shows great similarity to our solution I. We thus conclude that solution β' is consistent both in magnitude and phase with our data and correctly represents the true $\pi\pi \to \pi\pi$ scattering amplitude.

ACKNOWLEDGMENTS

It is a pleasure to acknowledge the important contributions made to the success of our experiment by R. Erichsen, C. Rey, M. Lawson, the Notre Dame scanning staff, and the Argonne streamer-chamber technical staff. Discussions with S. K. Bose, J. T. Donoghue, and N. Isgur were very helpful. This work has been supported by the National Science Foundation (Grant No. PHY-8007627) and by the U. S. Department of Energy, Division of Basic Energy Sciences.

*Present address: Bell Laboratories, Murray Hill, New Jersey.
†Present address: Fermi National Accelerator Laboratory, Batavia, Illinois.

[1]J. L. Petersen, CERN Report No. 77-04 (unpublished).
[2]E. Malamud and P. E. Schlein, Phys. Rev. Lett. 19, 1056 (1967).
[3]P. Estabrooks *et al.*, in *π-π Scattering—1973,* proceedings of the International Conference, Tallahassee, edited by P. K. Williams and V. Hagopian (AIP, New York, 1973), p. 37.
[4]B. Hyams *et al.*, Nucl. Phys. B64, 134 (1973).
[5]S. D. Protopopescu *et al.*, Phys. Rev. D 7, 1279 (1973).
[6]V. Srinivasan *et al.*, Phys. Rev. D 12, 681 (1975).
[7]P. Estabrooks and A. D. Martin, Nucl. Phys. B95, 322 (1975).
[8]B. Hyams *et al.*, Nucl. Phys. B100, 205 (1975).
[9]A. D. Martin and M. R. Pennington, Ann. Phys. (N.Y.) 114, 1 (1978).
[10]M. J. Corden *et al.*, Nucl. Phys. B157, 250 (1979).
[11]H. Becker *et al.*, Nucl. Phys. B151, 46 (1979).
[12]W. D. Apel *et al.*, Phys. Lett. 41B, 542 (1972).
[13]A. Skuja *et al.*, Phys. Rev. Lett. 31, 653 (1973).
[14]J. T. Carroll *et al.*, Phys. Rev. D 10, 1430 (1974).
[15]W. D. Apel *et al.*, Phys. Lett. 57B, 403 (1975).
[16]J. F. Grivaz *et al.*, Phys. Lett. 61B, 400 (1976).
[17]M. David *et al.*, Phys. Rev. D 16, 2027 (1977).
[18]W. D. Apel *et al.*, Nucl. Phys. B160, 42 (1979).
[19]G. Borreani *et al.*, Nucl. Phys. B187, 42 (1981).
[20]P. E. Cannata, Ph.D. Thesis, University of Notre Dame, 1980.
[21]N. M. Cason *et al.*, in *High Energy Physics—1980,* proceedings of the XX International Conference on High Energy Physics, edited by Loyal Durand and Lee G. Pondrom (AIP, New York, 1980), p. 5.
[22]N. N. Biswas *et al.*, Phys. Rev. Lett. 47, 1378 (1981).
[23]N. M Cason *et al.*, Phys. Rev. Lett. 48, 1316 (1982).
[24]A. E. Baumbaugh *et al.*, Nucl. Instrum. Methods 197, 297 (1982). See also A. E. Baumbaugh, Ph.D. Thesis, University of Notre Dame, 1981.
[25]Use of a thin (0.5-radiation-length) lead radiator followed by a 1-m^2 PWC did not improve this position resolution because of the problem of multiple hits in the PWC due to the fringe field of the magnet.
[26]F. T. Solmitz *et al.*, Alvarez programming note No. p-117 (unpublished).
[27]O. I. Dahl *et al.*, Alvarez programming note No. P-126 (unpublished).
[28]W. Hoogland *et al.*, Nucl. Phys. B69, 266 (1974).
[29]Particle Data Group, C. Bricman *et al.*, Phys. Lett. 75B, 115 (1978).
[30]S. Weinberg, Phys. Rev. Lett. 17, 616 (1966).
[31]G. E. Kalmus, in *Proceedings of the Conference on $\pi\pi$ and $K\pi$ Interactions,* edited by F. Loeffler and E. Malamud (Argonne National Laboratory, Argonne, Illinois, 1969) p. 413.
[32]G. Costa *et al.*, Nucl. Phys. B175, 402 (1980).
[33]R. J. Jaffe, Phys. Rev. D 15, 267, 281 (1977).
[34]S. K. Bose, Nuovo Cimento 46, 419 (1966); S. K. Bose and E. G. Sudarshan, Phys. Rev. 162, 1398 (1967).
[35]J. F. Donoghue, K. Johnson, and B. A. Li, Phys. Lett. 99B, 416 (1981).
[36]I. Cohen, N. Isgur, and H. J. Lipkin, Argonne Report No. ANL-HEP-PR-81-45, 1981 (unpublished); N. Isgur (private communication); J. F. Donoghue (private communication).